Multimillion Atom Simulations of Di-8-ANEPPS Chromophores Embedded in a Model Plasma Membrane

Bouquiaux, Charlotte; Champagne, Benoît; Beaujean, Pierre

Published in:
Journal of chemical information and modeling

DOI:
10.1021/acs.jcim.3c01568

Publication date:
2024

Document Version
Peer reviewed version

Multi-Million Atoms Simulations of Di-8-ANEPPS Chromophores Embedded in a Model Plasma Membrane: Towards the Investigation of Realistic Dyed Cell Membranes

Charlotte Bouquiaux, Benoît Champagne, and Pierre Beaujean*

University of Namur, Theoretical Chemistry Lab, Unit of Theoretical and Structural Physical Chemistry, Namur Institute of Structured Matter, rue de Bruxelles, 61, B-5000 Namur (Belgium)

E-mail: pierre.beaujean@unamur.be

Abstract

A multi-step computational approach has been employed to study a multi-million all-atom dyed plasma membrane, with no less than 42 different lipid species spanning the major head groups and a variety of fatty acids, as well as cholesterol, with the objective of investigating its structure and dynamics, as well as its impact on the embedded di-8-ANEPPS dyes. The latter are commonly-used bioimaging probes and serve as local microscopes. So, they provide information on membrane morphology via their second harmonic nonlinear optical (NLO) responses, which have the advantage of being specific to interface regions and sensitive to the chromophore environment. In previous studies, this chromophore has only been studied in simpler membrane models, far from the complexity of real lipid bilayers while, owing to the ever-increasing computational resources, a multi-million lipid bilayers has been studied, giving access to the effects of its heterogeneity. First, using molecular dynamics (MD) simulations, it is found that that the combination of lipids produces a more ordered and denser membrane compared to its homogeneous model counterparts, while the local environment of the embedded dyes becomes enriched in phosphatidylcholine. Subsequently, the second harmonic first hyperpolarizability of the probes has been calculated at the TDDFT level on selected frames of the MD, highlighting the influence of the lipid environment. Due to the complexity of the system, machine learning (ML) tools have been employed to establish relationships between the membrane structural parameters, the orientation of the probes and their NLO responses. These ML approaches have revealed influential features, including the presence of diaglycerol lipids close to the dye. As a whole, this work provides a first step toward understanding the cooperation, synergy, and interactions that occur in such complex guest-host environments, which have emerged as new targets for drug design and membrane lipid therapy.

1 Introduction

Biological membranes are ubiquitous structures in eukaryotic cells.[1] They define the cell boundaries and subdivide the interior of the cell by creating membranous compartments, such as the Golgi body, the endosomes and lysosomes, the mitochondria, or the endoplasmic reticulum.[2] All of them perform different and specialized functions.[3–5] Membranes separate the inside of the cell from the outside. The lipid membranes are often referred within the fluid mosaic model, a term introduced by Singer and Nicolson in 1972[6] to stress that the structure is both dynamic and ordered. Indeed, membrane domains, integral proteins, cytoskeletal and extracellular structures are responsible for the long-range and non-random organization, while smaller domains or lipid rafts maintain a certain dynamic flux across the membrane plane.[7] Each of them has characteristic lipids and proteins, and the relative proportions between the two differ with the type of membrane. In fact, the composition varies at all scales: between cells, between organelles, between membrane leaflets (leading to leaflet asymmetry), and even within a leaflet (forming rafts).[8] Considering the enormous variety of different lipid species available, one can begin to grasp the truly enormous complexity of such systems. Interestingly, modifications of the composition of membranes have been evidenced in some diseases, such as cancer, type 2 diabetes, Alzheimer's or Parkinson's diseases.[9–18] Thus, they are targets for new therapeutic approaches in the field of membrane lipid therapy (MLT).[2,19]

Experimental studies of the organization of cell membranes remain difficult because of the required high spatiotemporal resolution.[20] Fortunately, computer simulations can help filling in the missing pieces of information. Molecular modeling has proven to be a crucial tool to study the morphology of complex systems and provide real-time three-dimensional pictures of systems with atomistic resolution. The boost in available computational resources led to an increase of the size of the targeted systems. From the one- or two-component membranes of a few hundred atoms studied in the 1990s, millions of atoms can now be

included.[21] Thus, larger and more complex systems are now within reach. However, the study of biological-like membranes is still incomplete. Often only a few different lipid species are considered at a time,[22–31] even for larger lipid bilayers (LB).[32–34] Moreover, computer simulations have replaced all-atom (AA) descriptions with coarse-grain (CG) approaches in an attempt to limit the computational cost of large systems.[24,35] This makes it possible to study membrane structural changes on larger size and time scales, such as raft formation,[36,37] lipid flip-flop,[38,39] or membrane-protein interactions.[39,40] CG approaches are well suited in these cases, but not when the investigation requires detailed information about the flexibility, the conformation, or the geometry of the system components. This atomic resolution is especially necessary in multi-scale and multi-step approaches, where molecular dynamics (MD) simulations are performed first, followed by quantum mechanical (QM) calculations to address optical properties.

In the present work, MD simulations then QM/MM calculations are performed to investigate a model plasma membrane (PM) with embedded probe molecules, the di-8-ANEPPS dye. To our knowledge, this is the first multi-million AA MD simulation on chromophore-stained membranes. This all-atom model contains no less than 42 different lipid species, reflecting the diversity of polar headgroups and fatty acids of an ideal PM. They are asymmetrically distributed between the two leaflets to distinguish between the outer and inner lipid layers, with the ANEP staining the outer leaflet to reflect the situation immediately after its injection. The di-8-ANEPPS probe molecules, nested in the membrane as shown in Figure 1, serve as "local microscopes". The targeted optical response of those chromophores is the second harmonic generation (SHG), a second-order nonlinear optical (NLO) response that is highly sensitive to the symmetry,[41–43] and to the molecular environment,[44,45] so that they are markers of local membrane organization. Here, the SHG responses are evaluated at the hybrid QM/MM level. In this context, over the last decades, several studies have been carried out to design and/or to improve NLO chromophores as probes of biological media, and subsequently their use to investigate the membrane structure and organization.[46–50]

Specifically, the ANEP-like molecules are widely used as biocompatible optical probes to investigate membrane morphology[51–54] and membrane potential.[55–59] However, only a few theoretical investigations focused the SHG[60] or fluorescence[61–63] responses of di-8-ANEPPS in lipid membranes are available. These focus on analyzing the change of the optical signal in response to a variation of the membrane potential[60,62,63] and on comparing the absorption and emission spectra of di-8-ANEPPS in the gas phase and in the bilayer environment[61]. These studies account for the environmental and dynamical effects in different ways. So, Matson and co-workers[62] have reported TDDFT calculations of the spectral properties of the ANEP core of styryl dyes. The membrane environment is described using an implicit solvation model where non- or slightly polar solvents such as heptane and decanol represent the hydrocarbon region of the bilayer. These calculations do not take into account the dynamics of the system. Clark and co-workers[60] as well as Hirst and co-workers[61] have adopted a two-step computational approach, similar to that of the present investigation, starting with MD simulations of the dyed lipid bilayers, followed by QM/MM calculations to evaluate the optical responses: either at the SOS/CI level for the first hyperpolarizability[60], or at the TDDFT level for the fluorescence[61]. More recently, Youngworth and Roux[63] have performed MD simulations of dyed membranes where the di-8-ANEPPS probe is either in its ground or excited state. Absorption and emission energies were then directly determined as the difference of energies between these two states. Yet, in all those studies, only small lipid bilayers (up to 100 lipids) made of one or two components have been considered, thus far from the complexity of the biologically-relevant membranes studied in this work.

Previous MD studies by our group have focused on a single molecule of di-8-ANEPPS embedded in simple model membranes featuring single-component lipid bilayers.[31] It has been shown that the lipid organization is strongly dependent on the nature of the hydrophilic lipid head. For example, the orientation of a given lipid species varies depending on the nature of its polar head, which then influences the orientation of the embedded probe. Membrane structure is also influenced by the length and/or degree of unsaturation of the

fatty acids. Polyunsaturated lipid chains produce less ordered and less packed systems, whereas chain lengthening increases membrane order. Another study[64] has investigated the condensing effect of cholesterol by progressively increasing the cholesterol concentration in DPPC bilayers. The subsequent rigidity of the membrane was also evidenced and it was shown to move the orientation of the dyes towards the bilayer normal.

The massive system studied here allows us to assess how what has been observed in homogeneous models with respect to the influence of lipid building blocks on membrane structure and organization remains present in a complex lipid bilayer of mixed composition, or whether synergistic effects occur when these lipid species are combined. It is important to note that the expansion of compositional heterogeneity goes hand in hand with an increase

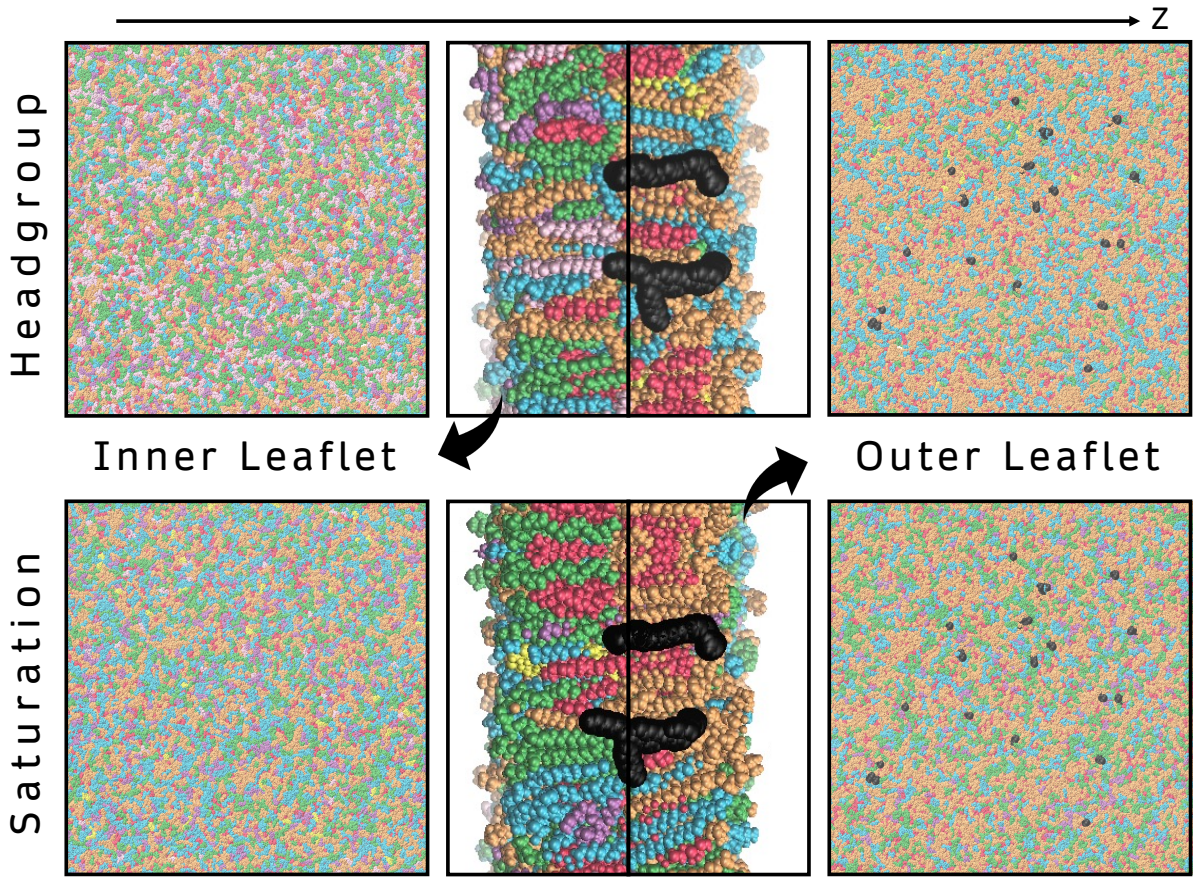

Figure 1: Diversity in lipid species and their asymmetric repartition between the inner and outer layers of the cell membrane [the meaning of the colors is discussed later. At this stage, they simply illustrate the heterogeneous composition], as well as initial positions of the 20 ANEPP probes [black].

in the number of factors to be considered and the complex relationships between them. Coupled with the extremely large trajectory files generated when studying multi-million atom systems, one can understand the appeal of automation and machine learning tools.[65,66] This illustrates the gradual shift that has occurred in computational chemistry over the last few decades, where the challenge has shifted from the feasibility of the calculations (in terms of the amount of computational resources available) to the processing and analysis of the simulated results. In addition to the membrane structural parameters, information about the embedded ANEP, its interactions with different lipid structures, its enhanced affinity towards certain species, its orientation and its geometry are also accessible. Moreover, little is known about the interactions between chromophores and their possible aggregation. The dynamics of their interactions is also studied. Thus, these results provide detailed information about both the dynamic organization of the plasma membranes, the composition and evolution of the immediate ANEP environment and its influence on the geometry, orientation and optical properties of the embedded probes.

2 Computational and Theoretical Methods

The two-step computational approach adopted in this work has already been tested and validated in our previous papers, which focus on single-component model membranes varying by their polar heads[31] or incorporationg cholesterol.[64] All the simulation details are therefore not reported here but are available from Refs. 31,64,67.

2.1 Membrane Construction

The composition of the membrane corresponds to that of an ideal PM[2,3,68] and was constructed using the CHARMM-GUI Membrane Builder.[69] It includes lipid species from all three major categories: glycerophospholipids (GPLs), sphingolipids (SLs), and sterols asymmetrically distributed between the inner (IL) and outer (OL) leaflets. 8 different types of

headgroups and 17 fatty acids are combined to form 42 different lipid species, representing a wide range of unsaturation (from 0 to 8 double bonds [DB]) and fatty acid length (from 16 to 24 carbon atoms). The zwitterionic phosphatidylcholine (PC), phosphatidylethanolamine (PE), and sphingomyelin (SM) are present in both leaflets, with PC and SM mainly in the OL and PE in the IL. Both lipid layers also contain the neutral diaglycerol (DAG), mainly in the OL, while the inner leaflet is enriched in charged species such as phosphatidylserine (PS), phosphatidylinotisol (PI), and phosphatidic acid (PA). Finally, cholesterol (CHL) tends to populate the OL, although it is present in both. The repartition of lipids in terms of headgroups and degree of unsaturation in the membranes is shown in Figure 2, and the full list of lipids included can be found in Table S1. Water molecules were added to both sides, as well as ions (K^+, Na^+, and Cl^-) to neutralize the system. Finally, 20 molecules of di-8-ANEPPS were randomly incorporated into the OL to simulate the situation immediately after injection. The complete stained and hydrated membrane is composed of 11261 lipids, 63250 water molecules, 6157 ions, and 20 chromophores (CHR), resulting in a system of over 3 million atoms and a size of $500\,\text{Å} \times 500\,\text{Å} \times 100\,\text{Å}$.

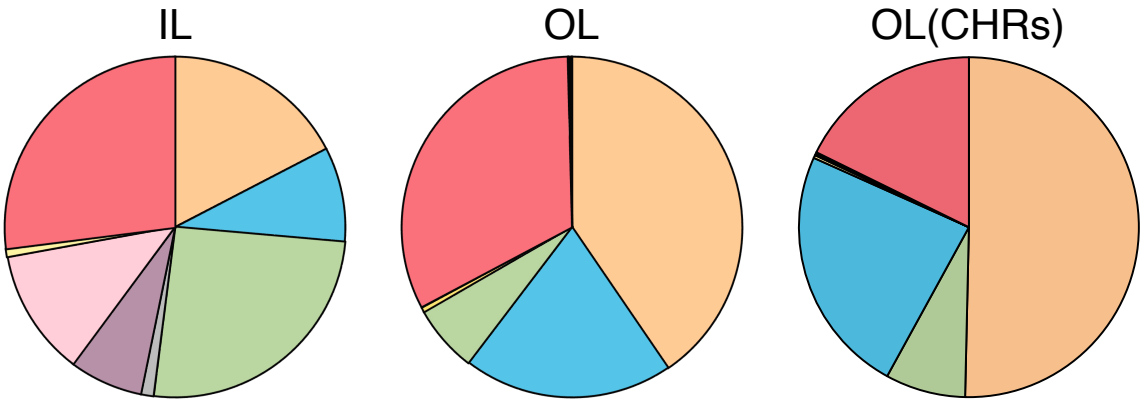

	%PC	%SM	%PE	%PS	%PI	%PA	%DAG	%CHL	%CHR
IL	17.40	9.00	25.60	12.0	7.00	1.2	0.80	27.00	0.00
OL	40.50	20.78	5.75	–	–	–	0.47	32.60	0.35
OL(CHRs)	51.01	23.54	7.56	–	–	–	0.28	17.61	0.35

(a)

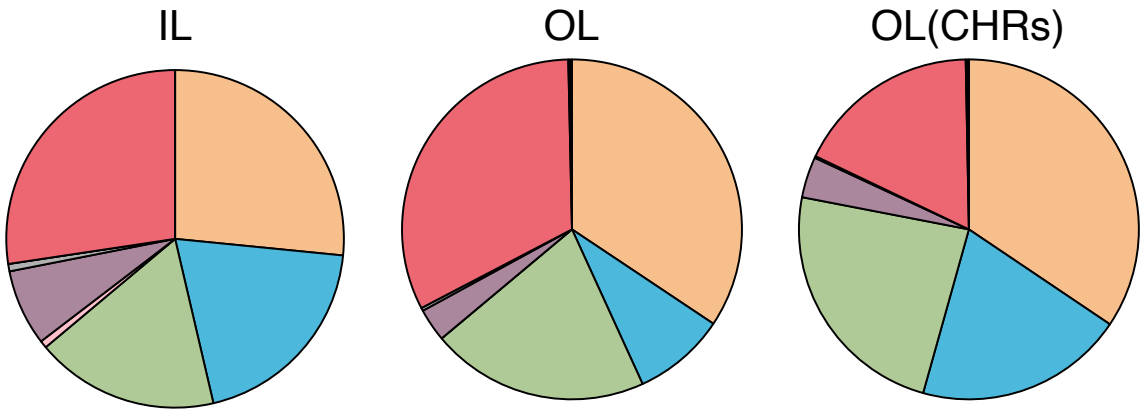

	%0DB	%1DB	%2DB	%3DB	%4DB	%6DB	%8DB	%CHL	%CHR
IL	26.57	19.78	17.55	0.71	7.30	0.71	0.00	27.00	0.00
OL	34.43	9.13	20.48	–	3.25	–	0.11	32.60	0.35
OL(CHRs)	34.74	19.91	23.69	–	3.88	–	0.17	17.61	0.35

(b)

Figure 2: Repartition of **(a)** the lipid headgroups, and **(b)** the degree of unsaturation between the inner (IL) and the outer (OL) leaflets, as well as the average composition 5.0 Å around the probes [OL(CHRs)] for the 25 snapshots extracted from the MD simulation.

2.2 Molecular Dynamics Simulations

The CHARMM36 (C36)[70,71] force field (FF) was used for the lipid molecules, TIP3P[72] for the water molecules, and a modified version of GAFF[67] for the chromophore. The MD simulations were performed with the NAMD[73] program following the CHARMM-GUI equilibration protocol. The 325 ns production run was performed in the NPT ensemble (P = 1 atm, T = 315.15 K), which is maintained using a Nosé-Hoover Langevin piston barostat[74] and a Langevin dynamic thermostat with a coupling constant of 1.0 ps. The Lennard-Jones interactions were truncated using a switching cutoff from 10 Å to 12 Å,[75] while the long-range Coulombic interactions were treated using the particle-mesh Ewald (PME) technique.[76] All simulations were performed with a time step of 2 fs. The technical details of the simulation can be found in the Supporting Information (Technical Aspects section).

2.3 Nonlinear Optical Properties Calculations

The calculations of the static and dynamic (λ = 1064 nm) NLO responses were performed at the TDDFT/M06-2X/6-311+G* level using the Gaussian16 package.[77] This choice of wavelength is supported by the fact that it lies within the therapeutic window[78–80]and that it is located between two absorption peaks of water[81] The M06-2X exchange-correlation functional exhibits an excellent general performance,[82] and in the case of the calculation of first hyperpolarizabilities, its predictions are in good agreement with experiment and/or with higher-level (wavefunction) methods thanks to its high percentage of exact Hartree-Fock exchange.[83–87] We focus on both the hyper-Rayleigh scattering (HRS) response, β_{HRS}, and the associated depolarization ratio (DR), as well as the diagonal β_{ZZZ} component of the first hyperpolarizability tensor, where Z is the direction normal to the bilayer. Complete expressions for β_{HRS} and DR can be found in Ref. 88. The NLO calculations were performed on 500 structures extracted from the MD production run (25 for each CHR, *i.e.* every 13 ns). The lipids surrounding the chromophore were accounted for by their electrostatic potential

(ESP) charges,[89,90] while the water molecules surrounding the ANEPPS@lipid system were accounted for using the integral equation formalism (IEF) of the polarizable continuum model (PCM).[91–93] Dynamic β_{HRS} values corrected by the homogeneous broadening model were also evaluated to remove unphysical resonant effects (see Refs. 67 and 64 for details). The vertical excitation energies of the chromophore were calculated as well using the same approximations, and used in frequency dispersion models in the treatment and analysis of the NLO responses.

2.4 Analysis Tools

2.4.1 Structural analysis

The evolution of both the total energy and the size of the simulation box were realized using VMD,[94] as well as the density profile graphs. The rest of the analysis (*i.e.* the evaluation of the area per lipid, the number of neighbors, the order parameter, the membrane curvature), was conducted with MDAnalysis[95,96] [which is a Python library designed to analyze trajectories from MD simulations] combined with the Lipyphilic Python toolkit.[97,98]

2.4.2 Relationships between features

The more complex the structure of the system, the more complex its detailed analysis. Indeed, due to the large number of factors (called features) at play, it is difficult to disentangle the effect of each (or each group) of them in order to reveal the influence of the local environment on the embedded probes. Therefore, we relied on the machine learning (ML) and data visualization tool Orange,[99] and more specifically on its FreeViz widget.[100] The latter is a visualization tool that evaluates linear projections and displays the projected data in a scatterplot to facilitate interpretation. Information about the relationships between features is also available. Looking at the resulting images (*e.g.* Figure 8), the lines from the origin are the projections of the feature base vectors and the circles are the data instances.

The longer the base vector, the more important it is for classifying the data instances. Also, the closest projections are the most correlated and *vice versa*. In some cases, to simplify the visualization, only features that extend beyond a certain distance from the center are displayed.

3 Results and Discussion

3.1 Bilayer Structural Parameters

The first goal here is to investigate the overall structure of this complex lipid bilayer as well as to highlight the nature of the different local environments of the embedded probes. Figure 3 presents the density profile of the different membrane components. The 20 di-8-ANEPPS molecules are interacting with the OL which is enriched in CHL, PC, SM, DAG, and PE, while the negatively charged PS, PI, and PA are only present in the IL. Moreover the chromophores penetrate deep into the membrane with their alkyl chains seeping into the other leaflet but they stay anchored in the OL. In practice, such anchoring allows a large enough time window to perform the NLO measurements because the SHG phenomenon requires an environment without a center of symmetry. Dyes with faster diffusion through the membrane will populate the IL, and progressively reduce the SHG signal.

By construction, the asymmetric repartition of lipid species between the leaflets, with the OL more enriched in CHL, makes the OL overall more packed. As no flip-flop is observed, the asymmetric density is conserved throughout the simulation and the average total area per lipid ($\langle A \rangle$) is $50.8 \pm 4.8\,\text{Å}^2$ ($51.7 \pm 3.8\,\text{Å}^2$) for the OL (IL). Considering the $\langle A \rangle$ values for the individual lipid (Table S2), globally, the lipid species produce more packed and denser environments (smaller $\langle A \rangle$ values) than in single-component lipid bilayers. Differences of about 10 to $20\,\text{Å}^2$ are observed. For example, a membrane composed only of DPPC lipids is characterized by $\langle A \rangle \sim 70\,\text{Å}^2$,[67] while for the complex LB a value of $\sim 52\,\text{Å}^2$ is found. This indicates that the combined influences of all the lipid species result in a higher general degree

of density that is adopted by all the lipid molecules. Nevertheless, the trends observed for the homogeneous systems are maintained: $\langle A \rangle$ decreases when lengthening the fatty acid chains, or, in the contrary, $\langle A \rangle$ increases when increasing the degree of unsaturation. On the other hand, for the SM family, the results are not really affected by the complexity of the system and differ by only $\sim 5\,\text{Å}^2$ compared to a full SM bilayer.[31] The least asymmetric lipid, SSM, is also the most densely packed. This is explained by its small tilt angle ($\sim 16°$). In fact, the denser environment is explained by the much higher orientation of the lipid tails in the mixed membrane compared to single-component bilayers. Taking DPPC as an example, the tilt angle, $\theta_{LIP_{CHAIN}}$, of about $\sim 30°$ in the full DPPC membrane is reduced by almost half ($\sim 17°$). In addition to the changes in the mean $\theta_{LIP_{CHAIN}}$ values, the standard deviations (SD) are also affected. The latter are significantly larger: for homogeneous systems, the SD is $\sim 10\%$ of the average, while in this case it is more than 50% of the average. Thus, although the highly heterogeneous membrane is more dense, it also induces a more dynamic character to the structure. The orientation of the lipid chains is globally more Z-aligned, but also more variable. Then, as for $\langle A \rangle$, the trends observed in simpler models are maintained

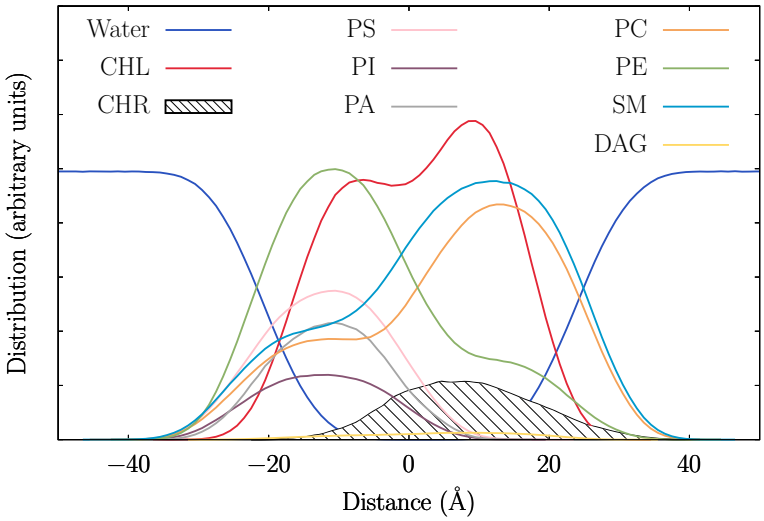

Figure 3: Normalized mass density profiles along the Z axis for the different components of the lipid bilayer. $z = 0$ defines the center of the bilayer. The OL is characterized by positive z values, the IL by negatives ones.

here. Lengthening the fatty acid chains decreases $\theta_{LIP_{CHAIN}}$, while adding one or more unsaturations increases $\theta_{LIP_{CHAIN}}$. This can be seen, for example, by looking at the variation in orientation between PSPE, POPE, and PLPE (Table S4). Also, because the leaflets are asymmetric, the same species do not have the same average orientation in both leaflets. Some are more Z-aligned in the OL, while others are more Z-aligned in the IL.

This asymmetric distribution, together with the shape of the lipid molecules causes the membrane to bend. The silhouette of the system is dynamic and fluctuates along the simulation, resulting in degrees of curvature changing with time and depending on the region of the system, as shown in Figures 4 and S2. The mean curvature for both leaflets (Figures 5a and 5b) shows that the regions of negative curvature (colored in red) in the IL leaflet match quite well those in the OL, and the same is observed for the regions of positive curvature (colored in gray), indicating that the changes in the surface topography are due to the evolution of the membrane curvature and not to a contraction or expansion of the membrane width. This is confirmed by the value of the average bilayer thickness, which, estimated from the distance between the phosphorus atoms in each leaflet (d_{P-P}), is 45.2 $\pm$ 0.1 Å. The small standard deviation indicates that although there is some waviness, the local thickness is not

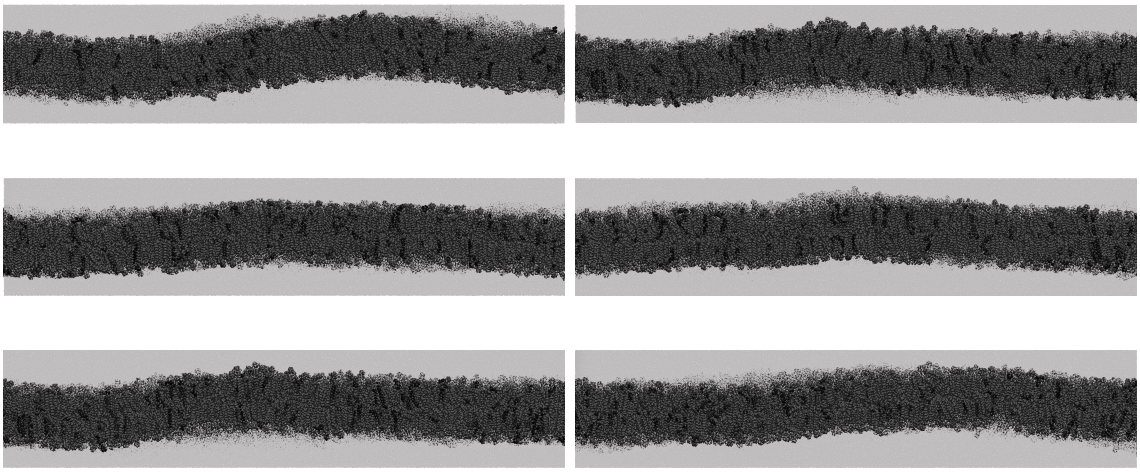

Figure 4: Membrane sideviews, taken at 0, 50, 100, 150, 200, 250 and 300 ns of the production run and illustrating the variations in curvature.

affected. Finally, the lipid chain order parameter (S_{CD}) is quite similar in both leaflets with an average S_{CD} value of 0.31 ± 0.07 (0.30 ± 0.10) for the IL (OL) (the individual values for each species can be found in Table S3). Furthermore, compared to examples provided in the Lipyphilic tutorials,[97,98] Figures 5c and 5d show barely no color variations, indicating that, based on the fatty acid order parameter, and in the timescale investigated here, there is no domain formation. This is confirmed when looking at the number of species in the largest cluster, which does not vary much. This is also true for the local environments of the probes indicating that the presence of the ANEP molecules does not have an impact of the neighboring membrane organization and the probes are surrounded by zones of varying degrees of (dis)order.

3.2 Di-8-ANEPPS Neighbors

After studying the overall shape of the system, the study focuses on the composition of the local environments of the probe and how they evolve in time. The 20 molecules of the chromophore are initially randomly positioned within the OL, as shown in Figure 6a. Initially, the di-8-ANEPPS molecules are located about 30 Å from each other, and as shown in Figure 6c, which shows the occupancy of di-8-ANEPPS throughout the production run, their positions do not fluctuate much. However, by looking at the evolution of the distances between the centers of mass (COM) of chromophore pairs along the simulation (Figure S3), they have the tendency to slowly drift towards each other. Compared to other membrane components, the CHR lateral diffusion is quite low. The diffusion coefficient, D, amounts to 0.21 ± 0.03 Å^2/ns, compared to, for instance, 6.38 ± 0.22 Å^2/ns and 5.90 ± 0.13 Å^2/ns for the DPPC in the OL and the whole OL, respectively. This indicates that, using the expression $t = r^2/2D$ where r if the distance travelled by the chromophores, aggregation would only occur after a time $t = \sim 2000$ ns if we consider $r = 30$ Å as the initial distances. The percentage presence of each species in a 5.0 Å radius around the probes can be found in the distribution plots (Figure S4), while the global average composition of each local

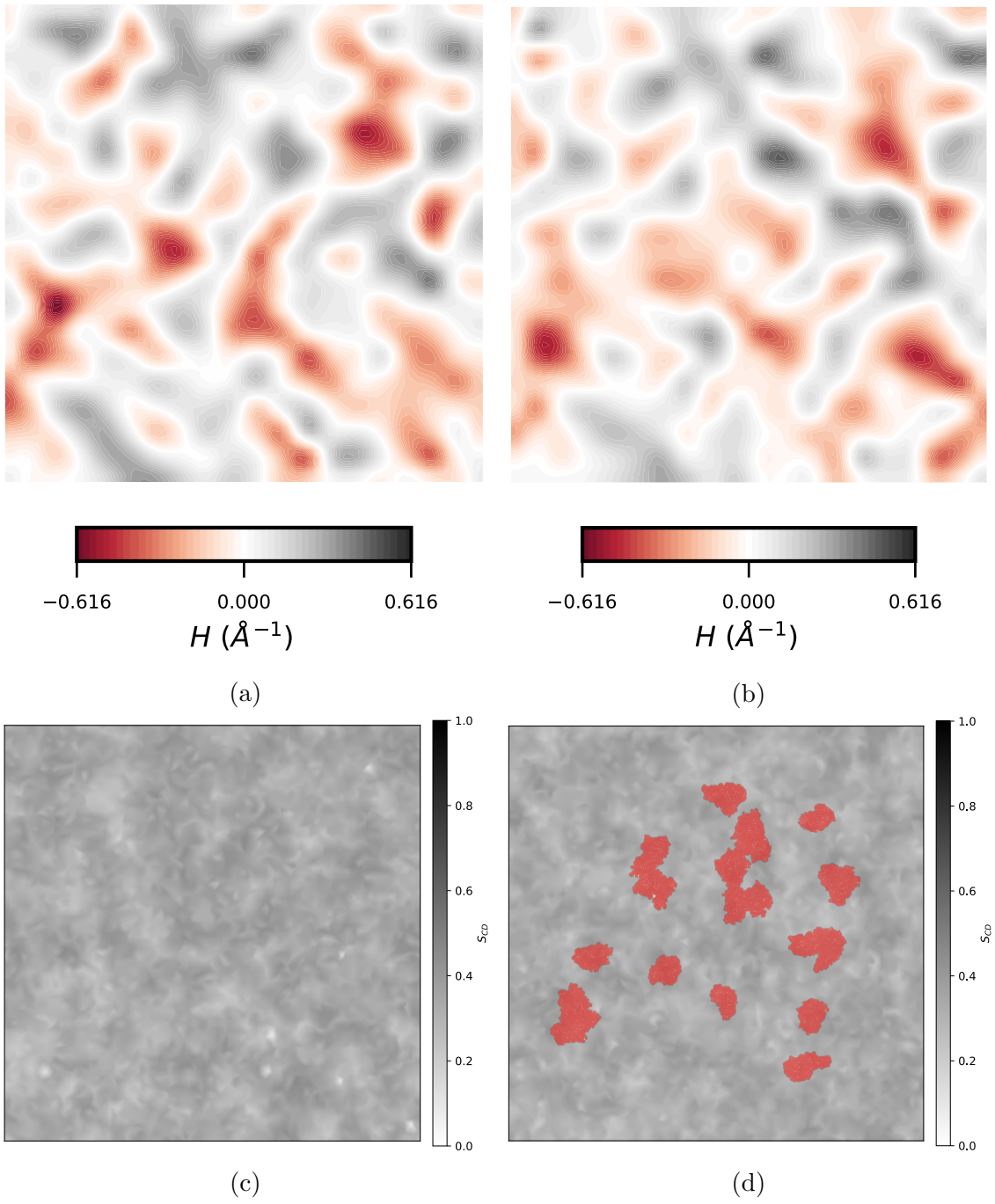

Figure 5: 2D mean curvature (Å^{-1}) in the **(a)** IL and **(b)** OL. 2D order parameter in the **(c)** IL and **(d)** OL with the CHR occupancy [red] superimposed to the graph.

environment in terms of individual lipid species, lipid headgroup, or degree of unsaturation is shown in Figures S5, S6, and S7, respectively. These graphs highlight the high degree of diversity in the local environments of the 20 probes. Comparing the average composition

of the environments surrounding the CHR with the global composition of the OL (Figure 2), it is found that the local environments of the 20 di-8-ANEPPS are enriched in SM and PE, and especially in PC. This is counterbalanced by the reduction by almost a factor of 2 of CHL, compared to the rest of the OL. Still, it represents more than 15% of the local environments. Note that, not all PC or SM lipids are more abundant in the CHRs immediate environments. For example, for the PC polar head, the presence of DGPC around the CHRs is multiplied by 3 with respect to the global OL composition, while it is more or less the same for DPPC, and it decreases by 10% for PSPC (Table S5). The most noticeable difference concerns the PLPE lipid, for which the average occupancy is almost 7 times higher when it is close to a probe. On the contrary, the local CHR environments are the most depleted in PSPE, POPC, DGPE and PLGL. Due to their low concentration, DAG molecules are only attracted to two of the 20 probes: DAGL around CHR14 and PLGL around CHR20. This results in a global depletion of DAG around CHR. More saturated lipids or lipids with a low degree of unsaturation are found in the vicinity of CHR, with the exception of DLiPC (with 4 unsaturations) around some di-8-ANEPPS and, as already mentioned, DAGL (with 8 unsaturations) around CHR14. Globally, the vicinity of CHR is enriched in mono-unsaturated lipids.

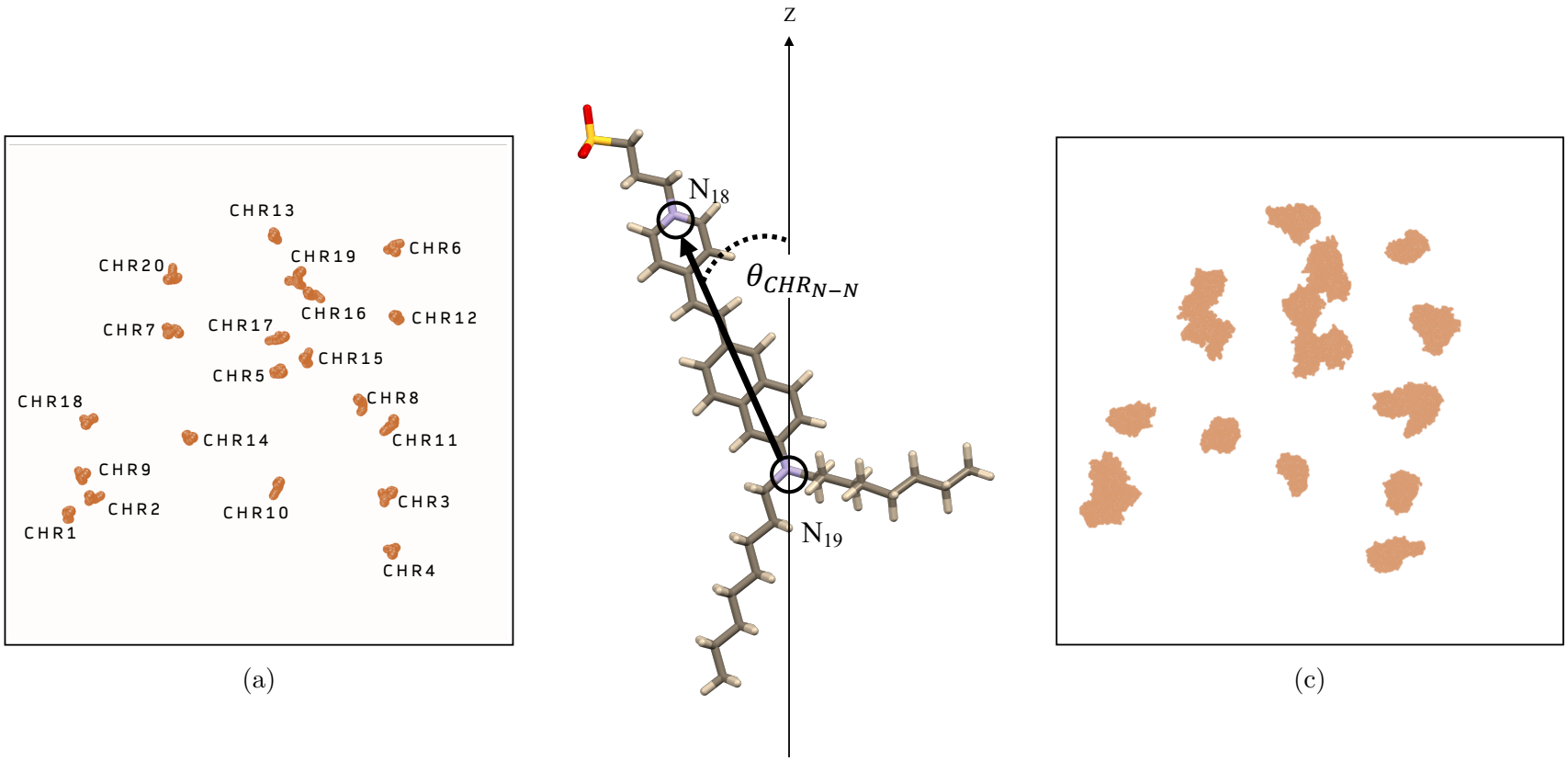

(a) (b) (c)

Figure 6: Di-8-ANEPPS **(a)** initial positions and **(b)** definition of the ANEP tilt angle as the angle formed by the vector connecting the N_{18} and N_{19} atoms and the normal to the bilayer interface (Z axis), and **(c)** overall occupancy within the OL.

3.3 Influence of the Lipid Environment on the Geometry and Orientation of the Probes

In this section, the influence of the different lipid environments on the structure of the chromophores and on their orientation in the bilayer is investigated. Key geometrical parameters of di-8-ANEPPS, namely, the bond length alternation (BLA) and torsion angles (all defined in Figure 7), are analyzed and compared. As shown for CHR1 (Figures S10 and S11), the geometrical parameters are influenced by each other and by the presence of some of the lipid species in the local environments. All the neighboring species of CHR1 [DPPC, POPC, DSM, NSM, PSM, SSM, and CHL (Figure S5a)] affect its conformation. This can be confirmed by looking at the important features that determine the geometrical parameters of another probe (Figures S13, and S14). Once again, the species neighboring CHR14 [PSM, DAGL, DEPC, DEPE, DGPC, DNPC, POPC, and CHL (Figure S5n)] are present in its FreeViz visualization. As mentioned in the previous Section, CHR14 is the only lipid surrounded by DAGL, the latter being quite an important feature influencing the BLA and the torsions angles. Since the surrounding CHR composition varies greatly from one probe to the next, the features that govern the geometrical parameters also vary, resulting in a wide range of values. The distribution plots of the geometrical parameters (Figure S8) show that the individual mean values vary little from each other (Table 1). The individual values vary between $-0.02\,$Å and $0.17\,$Å for BLA and between 150° and 180° for θ_1, θ_2 and θ_3. The average BLA is $\sim$ 0.07 Å, a value characteristic of a strong π electron delocalization between the donor and acceptor groups. The three torsion angles show values around 170° (with small standard deviations), indicating an out-of-plane distortion of about url = . The average ANEP neighborhood is mainly composed of PC, SM, and CHL, the latter having the largest influence on the key structural parameters. In particular, Figures S16 and S17 show that the nearby presence of DPPC, DNPC, SSM, PSM, and NSM are important features.

Regarding the probe orientation, $\theta_{CHR_{N-N}}$, (defined in Figure 6b), comparing the Free-

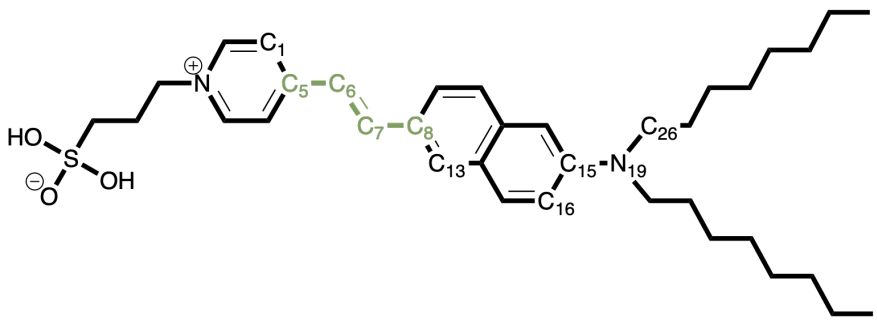

Figure 7: Chemical structure of di-8-ANEPPS with key atoms labeling, the segment used to define the bond length alternation (BLA $= \frac{1}{2}\left[d_{C_5-C_6} - 2d_{C_6-C_7} + d_{C_7-C_8}\right]$) of di-8-ANEPPS, and atoms used to define relevant torsion angles [$\theta_1 = \theta(C_1 - C_5 - C_6 - C_7)$, $\theta_2 = \theta(C_6 - C_7 - C_8 - C_{13})$, and $\theta_3 = \theta(C_{16} - C_{15} - N_{19} - C_{26})$].

Viz renderings for both CHR1 and CHR14 (Figures S12 and S15) show that $\theta_{CHR_{N-N}}$ is influenced by its surrounding lipids as well as its geometrical parameters. Considering the 20 CHRs, the same lipid species highlighted to influence the probe conformations (namely DPPC, DNPC, SSM, PSM, and NSM) are also important features determining the ANEP Z-alignment (Figure S18). For simpler single-component membranes, it has been shown that the probe follows the global orientation of the lipids. For example, in Ref. 64, the increase of the CHL concentration was associated with a progressive stiffening of the systems and the orientation of the DPPC lipids (and of ANEP). Overall, the variations of $\theta_{CHR_{N-N}}$ were related to the degree of order and packing of the different systems, allowing to establish a relationship between the composition of the lipid bilayer and the orientation of the chromophore. However, in the case of the present highly-heterogeneous system, the concentration in CHL around the chromophore (0.15 mole fraction) is too small to have a large impact on the orientation of the chromophore. This is consistent with other studies, which demonstrate changes of properties for larger concentration in CHL.[101,102] Overall~~In the case of the present highly heterogeneous system~~, the orientations of the lipids are not all correlated with each other (Figure 8), so there is no clear global orientation for the di-8-ANEPPS molecule to adopt. A wide range of $\theta_{CHR_{N-N}}$ is obtained: for CHR1 alone, individual $\theta_{CHR_{N-N}}$ values vary between 4° and 60° (Figure S9), while for all probes it ranges from 1° to 70°. Globally,

the probes do not have the same average orientation, contrary to what was observed for the (intramolecular) geometrical features: CHR10 (CHR3) is the most (least) aligned, with an average tilt angle of $17.5 \pm 10.3°$ ($32.5 \pm 16.0°$). The large standard deviations highlight the dynamic nature of the chromophore within the membrane. The neighboring lipids of these two probes are quite different, and CHR3 is more enriched in PC and not in SM compared to CHR10, and *vice versa*, while the percentage of surrounding CHL is similar. However, other ANEP with similar environments to either CHR3 or CHR10 do not show the same global orientation. The same conclusion can be drawn when looking at the degree of unsaturation of the lipids. Not one lipid is predominantly present around each probe, impacting the embedded ANEPPS. Therefore, it is not possible to disentangle the synergistic effect of all the different lipid molecules on the modulation of ANEP orientation. However, it is important to keep in mind that this is a model of a healthy PM in which the lipid species are more or less homogeneously distributed across a leaflet. This would not be the case in unhealthy tissue. For example, CHL concentration, which plays a major role in membrane order and fluidity, has been shown to be a key factor in cancer therapy resistance and metastasis.[103] By decreasing the CHL level, cells maximize their fluidity, allowing them to change their shape to be able to penetrate blood vessels.[14] On the contrary, increased levels of SM are associated with cancer initiation and growth.[104] Such changes in composition will then have a huge impact on the overall degree of packing and order within the membrane and, subsequently, the effect on the embedded probes will be perceived by variations in $\theta_{CHR_{N-N}}$.

Table 1: Di-8-ANEPPS tilt angle, $\theta_{CHR_{N-N}}$ (°), bond length alternation (BLA) (Å), and torsional angles (θ_1, θ_2, and θ_3) (°) (see Figures 6b and 7 for their definition), as well as their NLO properties: β_{HRS} and β_{ZZZ} ($\lambda = 1064\,\mathrm{nm}$) (in 10^3 a.u.). $\beta_{\mathrm{HRS/ZZZ}}^{1064nm-0.2}$ stands for the corrected quantities using the homogeneous damping and a damping factor, γ, of 0.2 eV.

	CHR1	CHR2	CHR3	CHR4	CHR5	CHR6	CHR7	CHR8	CHR9	CHR10
$\theta_{CHR_{N-N}}$	25.5 ± 15.7	25.0 ± 10.8	30.6 ± 15.0	18.8 ± 10.7	27.8 ± 13.7	20.0 ± 9.8	23.2 ± 11.2	25.0 ± 13.2	21.5 ± 10.6	18.3 ± 10.6
BLA	0.05 ± 0.02	0.07 ± 0.03	0.07 ± 0.03	0.07 ± 0.02	0.07 ± 0.03	0.07 ± 0.03	0.08 ± 0.03	0.07 ± 0.03	0.06 ± 0.04	0.06 ± 0.03
θ_1	169.1 ± 8.0	169.7 ± 8.1	169.0 ± 8.0	168.4 ± 5.9	170.6 ± 7.1	171.7 ± 7.4	167.6 ± 9.9	168.4 ± 9.7	167.9 ± 8.9	170.6 ± 6.4
θ_2	170.8 ± 7.0	170.7 ± 7.2	171.3 ± 6.8	171.0 ± 7.8	169.8 ± 6.8	171.6 ± 6.1	171.1 ± 7.4	172.5 ± 5.5	170.5 ± 5.8	171.1 ± 5.8
θ_3	168.2 ± 7.5	168.6 ± 8.3	168.9 ± 7.4	169.7 ± 6.0	168.1 ± 8.2	169.8 ± 5.9	168.9 ± 7.7	168.4 ± 7.1	168.0 ± 6.6	169.5 ± 6.8
$\beta_{\mathrm{HRS}}^{1064nm-0.2}$	154 ± 52	128 ± 61	143 ± 53	124 ± 59	136 ± 66	163 ± 51	152 ± 59	126 ± 56	146 ± 49	140 ± 57
$\beta_{\mathrm{ZZZ}}^{1064nm-0.2}$	-261 ± 135	-233 ± 111	-206 ± 104	-257 ± 141	-221 ± 149	-346 ± 149	-260 ± 108	-232 ± 133	-271 ± 107	-247 ± 188

	CHR11	CHR12	CHR13	CHR14	CHR15	CHR16	CHR17	CHR18	CHR19	CHR20
$\theta_{CHR_{N-N}}$	22.0 ± 11.8	26.7 ± 14.6	20.7 ± 11.7	24.6 ± 13.5	20.4 ± 9.9	25.4 ± 12.0	24.1 ± 15.1	24.6 ± 12.4	26.8 ± 12.7	22.7 ± 11.6
BLA	0.07 ± 0.04	0.07 ± 0.03	0.08 ± 0.04	0.05 ± 0.03	0.07 ± 0.03	0.07 ± 0.03	0.07 ± 0.03	0.07 ± 0.04	0.08 ± 0.03	0.06 ± 0.03
θ_1	168.0 ± .78	170.7 ± 7.3	169.8 ± 9.9	170.4 ± 6.9	170.2 ± 7.6	167.8 ± 6.7	166.6 ± 8.8	166.9 ± 11.6	171.3 ± 8.0	170.4 ± 9.2
θ_2	170.9 ± 6.8	171.5 ± 7.7	173.4 ± 7.2	171.5 ± 6.0	170.3 ± 7.5	171.5 ± 6.7	169.4 ± 7.9	169.9 ± 7.7	170.2 ± 5.6	171.1 ± 9.5
θ_3	171.4 ± 6.3	169.6 ± 6.5	168.7 ± 9.4	169.3 ± 7.6	171.0 ± 6.0	170.0 ± 7.8	168.8 ± 7.7	166.9 ± 9.0	167.8 ± 7.6	168.4 ± 5.9
$\beta_{\mathrm{HRS}}^{1064nm-0.2}$	158 ± 63	164 ± 63	161 ± 75	172 ± 66	140 ± 59	136 ± 66	159 ± 61	127 ± 42	136 ± 51	197 ± 226
$\beta_{\mathrm{ZZZ}}^{1064nm-0.2}$	-307 ± 163	-283 ± 135	-298 ± 162	-275 ± 149	-270 ± 125	-245 ± 141	-300 ± 144	-232 ± 95	-240 ± 107	-276 ± 170

In addition to the influence of neighboring lipids on CHR orientation, it is also interesting to look at the opposite effect and determine whether the CHRs perturb the local or global environment. The presence of a probe in their vicinity seems to slightly alter the lipid arrangement. First, comparing the average $\theta_{LIP_{CHAIN}}$ of each lipid in the whole OL with only the neighboring CHR lipids (Table S4) shows that most lipids are less aligned (mainly PLPC, DNPC, POPE, PLPE, and DGPE) when an ANEP is nearby. The difference is most noticeable for PLGL, which has a $\theta_{LIP_{CHAIN}}$ of 25.6 ± 18.9° globally, and 36.9 ± 30.0° around CHR20. In this case, the large standard deviation is explained by some cases where the PLGL is almost perpendicular to the bilayer normal. The opposite is observed for the other DAG lipid in OL. DAGL is much more aligned near CHR14 (21.0 ± 14.6°) than in the OL (31.9 ± 19.5°). Note also that the orientation of the CHL is not affected and is nearly identical when it is around the probes, globally in the OL or in the IL. Also, the average $\theta_{LIP_{CHAIN}}$ values for a given species are quite spread out. From one probe to the next, the results can vary by a factor of 2. For example, NSM shows an average orientation of 10.1 ± 6.3° (22.2 ± 11.1°) around CHR1 (CHR2).

3.4 Influence of the Lipid Environment on the NLO Responses

This Section focuses on the NLO responses of the embedded probes, both the orientational average response (β_{HRS}) and the response oriented along the bilayer normal (β_{ZZZ}) (Figure S19). Previous studies on collections of single-component membranes[31,64] have shown that it is not easy to relate variations in the β_{HRS} responses to changes in the lipid bilayer composition. For example, there was a slight increase in β_{HRS} when going from a pure DPPC bilayer to a system containing 12.5% CHL mole fraction, but this further increase in CHL concentration did not further enhance the signal. In addition, no clear trends emerged when looking at the variations of the NLO responses and the type, size, or charge of the polar heads. On the contrary, for β_{ZZZ} the signal increases as a consequence of a higher degree of order, forcing the alignment of the probe with the bilayer normal. Since the variations

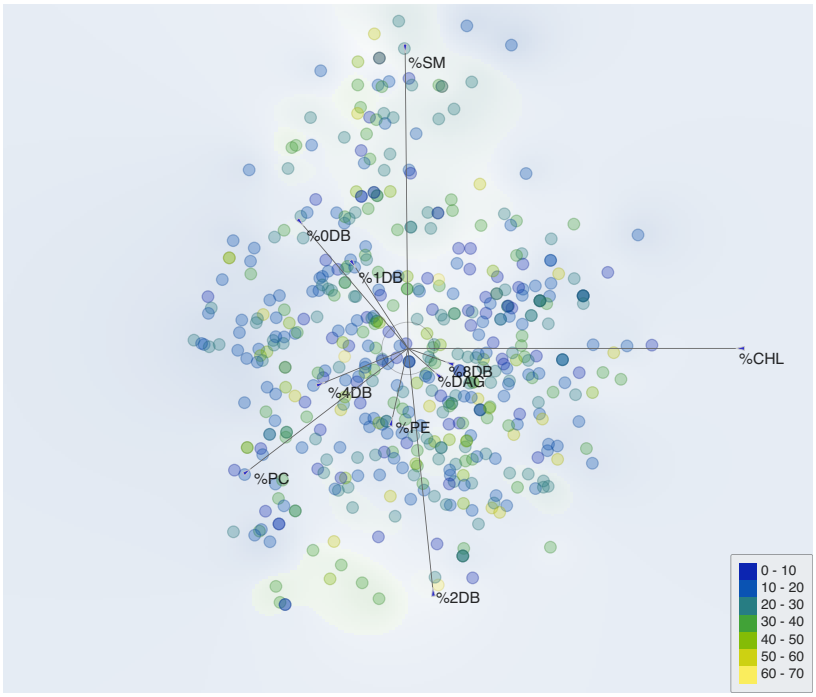

(a)

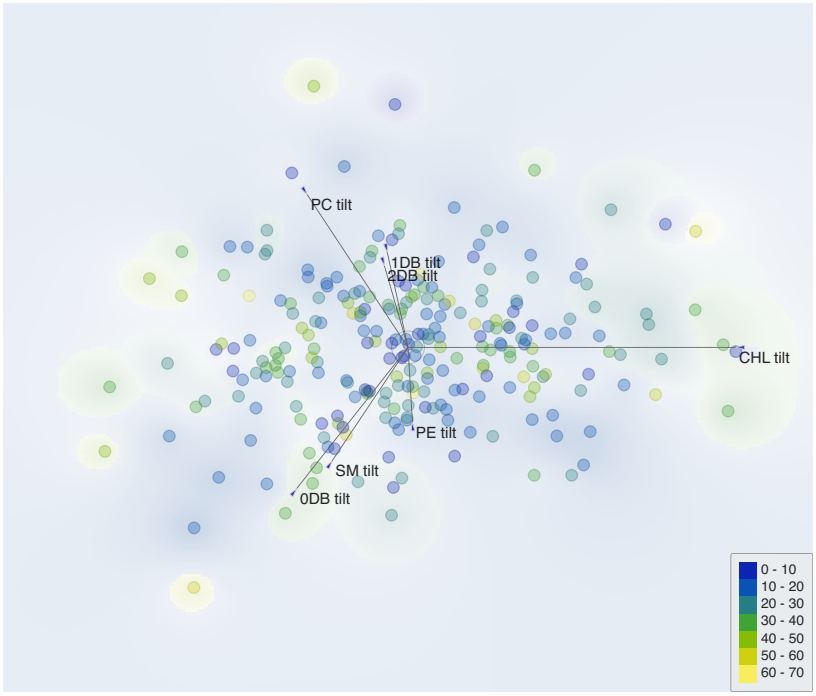

(b)

Figure 8: 20 CHRs: linear projections of the parameters taken as features for $\theta_{CHR_{N-N}}$ when considering: **(a)** the lipid composition (%), and **(b)** the Z-alignment of the lipid species (°) grouped by the nature of the polar head or by the degree of lipid tail unsaturation.

in lipid chain order could be associated with changes in membrane composition, the β_{ZZZ} signal was a good probe of this simple model environment. Also, in general, for both β_{HRS} and β_{ZZZ}, changes in the hydrophilic region had a greater effect on the membrane structural properties and NLO responses than varying the hydrocarbon center.

In the present study, the average β_{HRS} responses are approximately in the range of 150 10^3 a.u.. The large standard deviations, which highlight the dynamical nature of the system, are magnified by the presence of a few frames in resonant conditions, such as the value of 1203 10^3 a.u. obtained for CHR20. Without taking them into account, CHR4 (CHR14) has the largest (smallest) average β_{HRS} value with 124 10^3 $\pm$ 59 10^3 a.u. (172 10^3 a.u. $\pm$ 66 10^3 a.u.). Because the local environment of each probe is different, it is difficult to rationalize these results and relate them to bilayer and chromophore structural changes. In fact, as shown in Figure S20a, there are many factors at play here with the enormous diversity of lipid structures. Interestingly, the dynamic β_{HRS} ($\beta_{HRS}^{1064nm-0.2}$) results do not seem to be greatly affected by the static (β_{HRS}^{∞}) results, which are buried among all the other features. However, Figure S20b, which shows the lipid grouped by the nature of its hydrophilic and hydrophobic regions, shows that β_{HRS}^{∞} is indeed a determining factor. Streamlining the visualization by grouping and reducing the number of features allows hidden features to cut through the noise and become visible. It also reveals that both the nature of the lipid head and the structure of the lipid tails influence the β_{HRS} response. Interestingly, the percentage of DAG lipids, which are only present around 2 probes (CHR14 and CHR20), is an important feature: higher %DAG can be associated with larger $\beta_{HRS}^{1064nm-0.2}$ values. On the contrary, %PE is isolated from the other features and is associated with lower $\beta_{HRS}^{1064nm-0.2}$ responses. Regarding the lipid tails, the influence of polyunsaturated lipids is dominant compared to saturated species or lipids with low degree of unsaturation. The small contributions observed from %0DB and %1DB can be understood by looking at Figure S21a, which shows that lipids belonging to the 0DB category are not correlated features. This results in the small global effect on β_{HRS} seen in Figure S20a. As already highlighted in previous works,[105] both the

probe conformations and their degree of π-electron conjugation have large effects on the probe's NLO responses (Figure S21b).

The FreeViz visualizations (Figures 9a and 9b) for β_{ZZZ} display the same lipid species as for β_{HRS} as being important features, as well as the CHR geometrical parameters, and so the same level of complexity when analyzing them. The individual values vary between -864 10^3 a.u. and -13 10^3 a.u. without considering the resonant frames. Globally, the mean response is the largest (smallest) for CHR6 (CHR3) with -346 10^3 a.u. $\pm$ 149 10^3 a.u. (-206 10^3 a.u. $\pm$ 104 10^3 a.u.). CHR3 has already been singled out as the least aligned chromophore. By definition, the variations in $\beta_{\mathrm{ZZZ}}^{1064nm-0.2}$ is related to variations in the orientation of the dyes: small $\theta_{CHR_{N-N}}$ values are associated with large $\beta_{\mathrm{ZZZ}}^{1064nm-0.2}$ responses and *vice versa.* The correlation between β_{ZZZ} and $\theta_{CHR_{N-N}}$ is shown in Figure S23, where the third power and $\cos(\theta_{CHR_{N-N}})$ are used as abscissa because β is a rank 3 tensor. To relate changes in $\beta_{\mathrm{ZZZ}}^{1064nm-0.2}$ to changes in the lipid composition surrounding the CHR, the missing piece is the connection between $\theta_{CHR_{N-N}}$ and the lipid orientation (Figure 9b) and the lipid composition surrounding the ANEPPS. As mentioned above, this relationship is difficult to establish for this healthy PM model, which does not have any lipid clusters or domains. In fact, the 20 local environments are not sufficiently different in their composition. Again using the example of cancer cells, the associated lower CHL level would result in a decrease in $\theta_{CHR_{N-N}}$, and *vice versa* for the SM content. Departure of the CHR from Z-alignment will be detected by a decrease in the $\beta_{\mathrm{ZZZ}}^{1064nm-0.2}$ response.

4 Conclusions and Outlooks

A two-step MD-QM method has been used to study a multi-million all-atom lipid bilayer stained with chromophores. First, a detailed analysis of the structural parameters revealed that, compared to single-component membranes, the lipids, when mixed, assemble into a denser and more ordered membranes with more aligned lipids, while also inducing a more

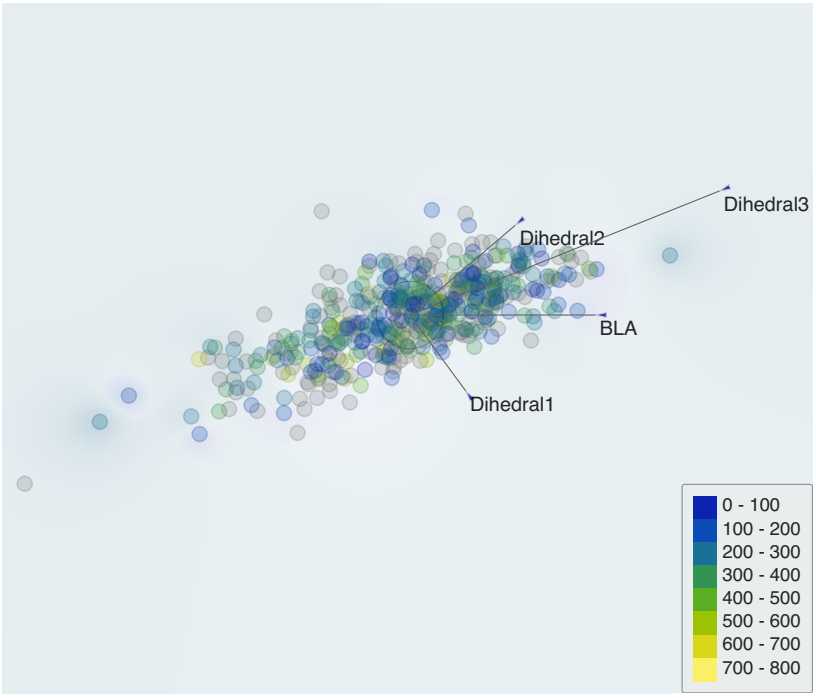

(a)

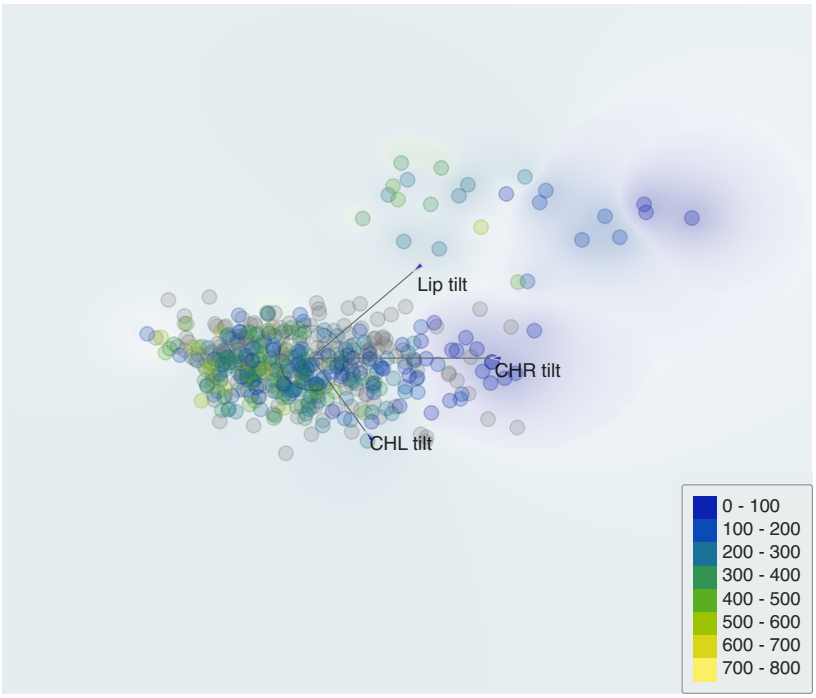

(b)

Figure 9: 20 CHRs: linear projections of the parameters taken as features for $\beta_{ZZZ}^{1064nm-0.2}$ (-10^3 a.u.), when considering **(a)** the probes geometrical parameters, and **(b)** the orientation of the membrane components (°).

dynamic character to the structure. Nevertheless, in addition to the individual values, the variations associated with a change in lipid nature are preserved: lengthening of the fatty acids causes a decrease (increase) in $\langle A \rangle$ (S_{CD}), while a higher degree of unsaturation produces the opposite effect. The asymmetric distribution of the lipids between the two leaflets causes them to have different structural parameters in the two layers, as well as to induce a slight curvature of the structure.

A detailed analysis of the dynamic nature of the lipids has highlighted that the direct ANEP environments are enriched in PC and SM specifically, and are more concentrated in saturated species or with low degree of unsaturation. Compared to the lipids, the position of the 20 chromophores does not fluctuate much and no aggregation is observed. Although the presence of the probes does not alter the global order of the membrane, it does cause the lipids in the vicinity to be less aligned with the bilayer normal than in the rest of the leaflet (cholesterol is hardly affected).

Since the immediate environment changes from one probe to the next, as well as dynamically, one can truly grasp the real complexity of biomembranes. Indeed, the number of factors to be taken into account makes it difficult to rationalize the variation in the structural parameters of the ANEP, its orientation, and its NLO properties. The lipids are not all oriented in the same direction, so there is no global orientation for the chromophores to adopt. Nevertheless, variations in β_{ZZZ} can be related to changes in chromophore orientation: an increase in β_{ZZZ} is associated with a more aligned ANEP.

The composition of a healthy membrane was used here as a model. In the future, lipid bilayers with compositions characteristic of a particular disease could be designed to further test the use of di-8-ANEPPS as a NLO probe of its environment and thus as a diagnostic tool.

Data Availability

For the MD simulations, the parameter files, the input file, the input configurations, and the output trajectory are available at https://doi.org/10.5281/zenodo.8321602. The commercial versions of NAMD and Gaussian codes were used.

Supporting Information Available

Details on: **(A)** the technical aspects of the MD simulations. **(B)** the membrane morphology: (i) the membrane construction (Figure S1), (ii) the system equilibration (Figure S1), (iii) the area per lipid (Figure S2), (iv) the order parameter (Figure S3), (v) the lipid orientation (Figure S4), and (vi) the membrane curvature (Figure S2). **(C)** the di-8-ANEPPS neigbhors: (i) the distances between chromophores (Figure S3), (ii) distribution graphs (Figure S4), and (iii) the average local environments (Figures S5-S7 and Table S5). **(D)** the di-8-ANEPPS geometrical parameters: (i) distribution graphs of the geometrical parameters (Figure S8) and chromophore orientation (Figure S9f), and (ii) linear projections (Figures S10-S18). **(E)** the nonlinear optical properties: (i) distribution graphs (Figure S19), and (ii) linear projections (Figures S20-S22).

Author Information

Corresponding author

Pierre Beaujean Theoretical Chemistry Laboratory, Unit of Theoretical and Structural Physical Chemistry, Namur Institute of Structured Matter, University of Namur, B-5000 Namur, Belgium; orcid.org/0000-0003-3723-3257

Authors

Charlotte Bouquiaux Theoretical Chemistry Laboratory, Unit of Theoretical and Structural Physical Chemistry, Namur Institute of Structured Matter, University of Namur, B-5000 Namur, Belgium; orcid.org/0000-0002-3335-0264

Benoît Champagne Theoretical Chemistry Laboratory, Unit of Theoretical and Structural Physical Chemistry, Namur Institute of Structured Matter, University of Namur, B-5000 Namur, Belgium; orcid.org/0000-0003-3678-8875

Notes

The authors declare no competing financial interest.

Acknowledgements

C.B. thanks Prof. F. Castet, Prof. F. Cecchet, Prof. M. Deleu, Prof. Y. Olivier, Dr. L. Le Bras, and Dr. T. N. Ramos, for fruitful discussions. C.B. thanks the F.R.S.-FNRS for her FRIA fellowship. P.B. is grateful to the EuroCC project (H2020-JTI-EuroHPC-2019-2, project number: 951732) for funding, which allowed the integration of the software in the different computing environments. The calculations were performed on:(i) the computers of the Consortium des Équipements de Calcul Intensif (CÉCI, http://www.ceci-hpc.be) and particularly those of the Technological Platform of High-Performance Computing, for which the authors gratefully acknowledge the financial support of the FNRS-FRFC, of the Walloon Region, and of the University of Namur (Conventions No. 2.5020.11, U.G006.15, U.G018.19, U.G011.22, 1610468, and RW/GEQ2016), (ii) on Zenobe, the Tier-1 facility of the Walloon Region (Convention 1117545), and (iii) on the LUMI supercomputer, which is owned by the EuroHPC Joint Undertaking, hosted by CSC (Finland). We acknowledge the LUMI con-

sortium through a LUMI-BE Regular Access call for awarding the project computing time. LUMI-BE is a joint effort from BELSPO (federal), SPW Économie Emploi Recherche (Wallonia), Department of Economy, Science & Innovation (Flanders), and Innoviris (Brussels).

References

(1) Israelachvili, J. N.; Marcelja, S.; Horn, R. G.; Israelachvili, J. N. Physical Principles of Membrane Organization. *Q. Rev. Biophys.* **1980**, *13*, 121–200.

(2) Casares, D.; Escribá, P. V.; Rosselló, C. A. Membrane Lipid Composition: Effect on Membrane and Organelle Structure, Function and Compartmentalization and Therapeutic Avenues. *Int. J. Mol. Sci.* **2019**, *20*, 2167.

(3) Van Meer, G.; Voelker, D. R.; Feigenson, G. W. Membrane Lipids: Where they Are and How they Behave. *Nat. Rev. Mol. Cell Biol.* **2008**, *9*, 112–124.

(4) Shevchenko, A.; Simons, K. Lipidomics: Coming to Grips with Lipid Diversity. *Nat. Rev. Mol. Cell Biol.* **2010**, *11*, 593–598.

(5) Harayama, T.; Riezman, H. Understanding the Diversity of Membrane Lipid Composition. *Nat. Rev. Mol. Cell Biol.* **2018**, *19*, 281–296.

(6) Singer, S. J.; Nicolson, G. L. The Fluid Mosaic Model of the Structure of Cell Membranes. *Science* **1972**, *175*, 720–731.

(7) Nicolson, G. L. The Fluid-Mosaic Model of Membrane Structure: Still Relevant to Understanding the Structure, Function and Dynamics of Biological Membranes After More than 40 Years. *Biochim. Biophys. Acta Biomembr.* **2014**, *1838*, 1451–1466.

(8) Nelson, D. L.; Cox, M. M. *Principle of Biochemistry*, 6th ed.; W. H. Freeman and Company: New-York, 2013.

(9) Michel, V.; Bakovic, M. Lipid Rafts in Health and Disease. *Biol. Cell* **2007**, *99*, 129–140.

(10) Farooqui, A. A. Lipid Mediators in the Neural Cell Nucleus: their Metabolism, Signaling, and Association with Neurological Disorders. *Neuroscientist* **2009**, *15*, 392–407.

(11) Marin, R.; Rojo, J. A.; Fabelo, N.; Fernandez, C. E.; Diaz, M. Lipid Raft Disarrangement as a Result of Neuropathological Progresses: a Novel Strategy for Early Diagnosis? *Neuroscience* **2013**, *245*, 26–39.

(12) Baenke, F.; Peck, B.; Miess, H.; Schulze, A. Hooked on Fat: the Role of Lipid Synthesis in Cancer Metabolism and Tumour Development. *DMM Dis. Model. Mech.* **2013**, *6*, 1353–1363.

(13) Gray, S. M.; Aylor, K. W.; Barrett, E. J. Unravelling the Regulation of Insulin Transport Across the Brain Endothelial Cell. *Diabetologia* **2017**, *60*, 1512–1521.

(14) Szlasa, W.; Zendran, I.; Zalesińska, A.; Tarek, M.; Kulbacka, J. Lipid Composition of the Cancer Cell Membrane. *J. Bioenerg. Biomembr.* **2020**, *52*, 321–342.

(15) Hussain, G.; Anwar, H.; Rasul, A.; Imran, A.; Qasim, M.; Zafar, S.; Imran, M.; Kamran, S. K. S.; Aziz, N.; Razzaq, A.; Ahmad, W.; Shabbir, A.; Iqbal, J.; Baig, S. M.; Ali, M.; Gonzalez de Aguilar, J. L.; Sun, T.; Muhammad, A.; Muhammad Umair, A. Lipids as Biomarkers of Brain Disorders. *Crit. Rev. Food Sci. Nutr.* **2020**, *60*, 351–374.

(16) Buchet, R.; Pikuła, S. Alzheimer's Disease: its Origin at the Membrane, Evidence and Questions. *Acta Biochim. Pol.* **2000**, *47*, 725–733.

(17) Kao, Y.-c.; Ho, P.-c.; Tu, Y.-k.; Jou, I.-m.; Tsai, K.-j. Lipids and Alzheimer's Disease. *Int. J. Mol. Sci.* **2020**, *21*, 1505.

(18) Vasseur, S.; Guillaumond, F. Lipids in Cancer: A Global View of the Contribution of Lipid Pathways to Metastatic Formation and Treatment Resistance. *Oncogenesis* **2022**, *11*, 46.

(19) Preta, G. New Insights Into Targeting Membrane Lipids for Cancer Therapy. *Front. Cell Dev. Biol.* **2020**, *8*, 1–10.

(20) Page, E. F.; Blake, M. J.; Foley, G. A.; Calhoun, T. R. Monitoring Membranes: the Exploration of Biological Bilayers with Second Harmonic Generation. *Chem. Phys. Rev.* **2022**, *3*, 041307.

(21) Marrink, S. J.; Corradi, V.; Souza, P. C.; Ingólfsson, H. I.; Tieleman, D. P.; Sansom, M. S. Computational Modeling of Realistic Cell Membranes. *Chem. Rev.* **2019**, *119*, 6184–6226.

(22) Vácha, R.; Berkowitz, M. L.; Jungwirth, P. Molecular Model of a Cell Plasma Membrane With an Asymmetric Multicomponent Composition: Water Permeation and Ion Effects. *Biophys. J.* **2009**, *96*, 4493–4501.

(23) Jo, S.; Lim, J. B.; Klauda, J. B.; Im, W. CHARMM-GUI Membrane Builder for Mixed Bilayers and Its Application to Yeast Membranes. *Biophys. J.* **2009**, *97*, 50–58.

(24) de Jong, D. H.; Lopez, C. A.; Marrink, S. J. Molecular View on Protein Sorting into Liquid-Ordered Membrane Domains Mediated by Gangliosides and Lipid Anchors. *Faraday Discuss.* **2013**, *161*, 347–363.

(25) Wu, E. L.; Fleming, P. J.; Yeom, M. S.; Widmalm, G.; Klauda, J. B.; Fleming, K. G.; Im, W. E. coli Outer Membrane and Interactions with OmpLA. *Biophys. J.* **2014**, *106*, 2493–2502.

(26) Malta de Sá, M.; Sresht, V.; Rangel-Yagui, C. O.; Blankschtein, D. Understanding Miltefosine–Membrane Interactions Using Molecular Dynamics Simulations. *Langmuir* **2015**, *31*, 4503–4512.

(27) Baoukina, S.; Rozmanov, D.; Tieleman, D. P. Composition Fluctuations in Lipid Bilayers. *Biophys. J.* **2017**, *113*, 2750–2761.

(28) Shahane, G.; Ding, W.; Palaiokostas, M.; Orsi, M. Physical Properties of Model Bi-

ological Lipid Bilayers: Insights from All-Atom Molecular Dynamics Simulations. *J. Mol. Model.* **2019**, *25*, 76.

(29) Osella, S.; Knippenberg, S. The Influence of Lipid Membranes on Fluorescent Probes' Optical Properties. *Biochim. Biophys. Acta Biomembr.* **2021**, *1863*, 183494.

(30) Dickson, C. J.; Walker, R. C.; Gould, I. R. Lipid21: Complex Lipid Membrane Simulations with AMBER. *J. Chem. Theory Comput.* **2022**, *18*, 1726–1736.

(31) Bouquiaux, C.; Castet, F.; Champagne, B. Influence of the Nature of the Lipid Building Blocks on the Second-Order Nonlinear Optical Responses of an Embedded Di-8-ANEPPS Probe. *J. Phys. Chem. B* **2023**, *127*, 528–541.

(32) Ganesan, N.; Taufer, M.; Bauer, B.; Patel, S. FENZI: GPU-Enabled Molecular Dynamics Simulations of Large Membrane Regions Based on the CHARMM Force Field and PME. 2011 IEEE Int. Symp. Parallel Distrib. Process. Work. Phd Forum. 2011; pp 472–480.

(33) Chavent, M.; Reddy, T.; Goose, J.; Dahl, A. C. E.; Stone, J. E.; Jobard, B.; Sansom, M. S. P. Methodologies for the Analysis of Instantaneous Lipid Diffusion in MD Simulations of Large Membrane Systems. *Faraday Discuss.* **2014**, *169*, 455–475.

(34) Patel, D. S.; Re, S.; Wu, E. L.; Qi, Y.; Klebba, P. E.; Widmalm, G.; Yeom, M. S.; Sugita, Y.; Im, W. Dynamics and Interactions of OmpF and LPS: Influence on Pore Accessibility and Ion Permeability. *Biophys. J.* **2016**, *110*, 930–938.

(35) Ingólfsson, H. I.; Melo, M. N.; van Eerden, F. J.; Arnarez, C.; Lopez, C. A.; Wassenaar, T. A.; Periole, X.; de Vries, A. H.; Tieleman, D. P.; Marrink, S. J. Lipid Organization of the Plasma Membrane. *J. Am. Chem. Soc.* **2014**, *136*, 14554–15449.

(36) Toppozini, L.; Meinhardt, S.; Armstrong, C. L.; Yamani, Z.; Kučerka, N.; Schmid, F.;

Rheinstädter, M. C. Structure of Cholesterol in Lipid Rafts. *Phys. Rev. Lett.* **2014**, *113*, 228101.

(37) Wassall, S. R.; Leng, X.; Canner, S. W.; Pennington, E. R.; Kinnun, J. J.; Cavazos, A. T.; Dadoo, S.; Johnson, D.; Heberle, F. A.; Katsaras, J.; Shaikh, S. R. Docosahexaenoic Acid Regulates the Formation of Lipid Rafts: a Unified View from Experiment and Simulation. *Biochim. Biophys. Acta - Biomembr.* **2018**, *1860*, 1985–1993.

(38) Bennett, W. F. D.; MacCallum, J. L.; Hinner, M. J.; Marrink, S. J.; Tieleman, D. P. Molecular View of Cholesterol Flip-Flop and Chemical Potential in Different Membrane Environments. *J. Am. Chem. Soc.* **2009**, *131*, 12714–12720.

(39) Thallmair, S.; Ingólfsson, H. I.; Marrink, S. J. Cholesterol Flip-Flop Impacts Domain Registration in Plasma Membrane Models. *J. Phys. Chem. Lett.* **2018**, *9*, 5527–5533.

(40) Charlier, L.; Louet, M.; Chaloin, L.; Fuchs, P.; Martinez, J.; Muriaux, D.; Favard, C.; Floquet, N. Coarse-Grained Simulations of the HIV-1 Matrix Protein Anchoring: Revisiting its Assembly on Membrane Domains. *Biophys. J.* **2014**, *106*, 577–585.

(41) Verbiest, T.; Clays, K.; Rodriguez, V. *Second-Order Nonlinear Optical Characterization Techniques: an Introduction*; CRC Press: Boca Raton, 2009.

(42) Meulenaere, E. D.; Bich, N. N.; de Wergifosse, M.; Hecke, K. V.; Meervelt, L. V.; Vanderleyden, J.; Champagne, B.; Clays, K. Improving the Second-Order Nonlinear Optical Response of Fluorescent Proteins: The Symmetry Argument. *J. Am. Chem. Soc.* **2013**, *135*, 4061–4069.

(43) de Wergifosse, M.; de Ruyck, J.; Champagne, B. How the Second-Order Nonlinear Optical Response of the Collagen Triple Helix Appears: A Theoretical Investigation. *J. Phys. Chem. C* **2014**, *118*, 8595–8602.

(44) Seidler, T.; Stadnicka, K.; Champagne, B. Second-order Nonlinear Optical Susceptibilities and Refractive Indices of Organic Crystals from a Multiscale Numerical Simulation Approach. *Adv. Optical Mater* **2014**, *2*, 1000–1006.

(45) Tonnelé, C.; Champagne, B.; Muccioli, L.; Castet, F. Nonlinear Optical Contrast in Azobenzene-Based Self-Assembled Monolayers. *Chem. Mater.* **2019**, *31*, 6759–6769.

(46) Alain, V.; Blanchard-Desce, M.; Ledoux-Rak, I.; Zyss, J. Amphiphilic Polyenic Push–Pull Chromophores for Nonlinear Optical Applications. *Chem. Commun.* **2000**, 353–354.

(47) Blanchard-Desce, M. H.; Ventelon, L.; Charier, S.; Moreaux, L.; Mertz, J. Molecular Probes for Nonlinear Optical Imaging of Biological Membranes. Linear and Nonlinear Optics of Organic Materials. 2001; pp 20–32.

(48) López-Duarte, I.; Chairatana, P.; Wu, Y.; Pérez-Moreno, J.; Bennett, P. M.; Reeve, J. E.; Boczarow, I.; Kaluza, W.; Hosny, N. A.; Stranks, S. D.; Nicholas, R. J.; Clays, K.; Kuimova, M. K.; Anderson, H. L. Thiophene-Based Dyes for Probing Membranes. *Org. Biomol. Chem.* **2015**, *13*, 3792–3802.

(49) Tran, R. J.; Sly, K. L.; Conboy, J. C. Applications of Surface Second Harmonic Generation in Biological Sensing. *Annu. Rev. Anal. Chem.* **2017**, *10*, 387–414.

(50) Osella, S.; Paloncýová, M.; Sahi, M.; Knippenberg, S. Influence of Membrane Phase on the Optical Properties of DPH. *Molecules* **2020**, *25*, 4264.

(51) Campagnola, P. J.; Wei, M.-d.; Lewis, A.; Loew, L. M. High-Resolution Nonlinear Optical Imaging of Live Cells by Second Harmonic Generation. *Biophys. J.* **1999**, *77*, 3341–3349.

(52) DiFranco, M.; Quinonez, M.; Capote, J.; Vergara, J. DNA Transfection of Mammalian Skeletal Muscles Using In Vivo Electroporation. *J. Vis. Exp.* **2009**, e1520.

(53) Reeve, J. E.; Anderson, H. L.; Clays, K. Dyes for Biological Second Harmonic Generation Imaging. *Phys. Chem. Chem. Phys.* **2010**, *12*, 13484–13498.

(54) Khadria, A.; de Coene, Y.; Gawel, P.; Roche, C.; Clays, K.; Anderson, H. L. Push–Pull Pyropheophorbides for Nonlinear Optical Imaging. *Org. Biomol. Chem.* **2017**, *15*, 947–956.

(55) Fluhler, E.; Burnham, V. G.; Loew, L. M. Spectra, Membrane Binding, and Potentiometric Reponses of New Charge Shift Probes. *Biochemistry* **1985**, *24*, 5749–5755.

(56) Loew, L. M. Potentiometric Dyes: Imaging Electrical Activity of Cell Membranes. *Pure Appl. Chem.* **1996**, *68*, 1405–1409.

(57) Obaid, A.; Loew, L.; Wuskell, J.; Salzberg, B. Novel Naphthylstyryl-Pyridinium Potentiometric Dyes Offer Advantages for Neural Network Analysis. *J. Neurosci. Methods* **2004**, *134*, 179–190.

(58) Pucihar, G.; Kotnik, T.; Miklavčič, D. Measuring the Induced Membrane Voltage with Di-8-ANEPPS. *J. Vis. Exp.* **2009**, e1659.

(59) Youngworth, R.; Roux, B. Simulating the Voltage-Dependent Fluorescence of Di-8-ANEPPS in a Lipid Membrane. *J. Phys. Chem. Lett.* **2023**, *14*, 8268–8276.

(60) Rusu, C. F.; Lanig, H.; Othersen, O. G.; Kryschi, C.; Clark, T. Monitoring Biological Membrane-Potential Changes: A CI QM/MM Study. *J. Phys. Chem. B* **2008**, *112*, 2445–2455.

(61) Robinson, D.; Besley, N. A.; O'Shea, P.; Hirst, J. D. Di-8-ANEPPS Emission Spectra in Phospholipid/Cholesterol Membranes: A Theoretical Study. *J. Phys. Chem. B* **2011**, *115*, 4160–4167.

(62) Matson, M.; Carlsson, N.; Beke-Somfai, T.; Nordén, B. Spectral Properties and

Orientation of Voltage-Sensitive Dyes in Lipid Membranes. *Langmuir* **2012**, *28*, 10808–10817.

(63) Youngworth, R.; Roux, B. Simulating the Voltage-Dependent Fluorescence of Di-8-ANEPPS in a Lipid Membrane. *J. Phys. Chem. Lett.* **2023**, *14*, 8268–8276.

(64) Bouquiaux, C.; Castet, F.; Champagne, B. Unravelling the Effects of Cholesterol on the Second-Order Nonlinear Optical Responses of Di-8-ANEPPS Dye Embedded in Phosphatidylcholine Lipid Bilayers. *J. Phys. Chem. B* **2021**, *125*, 10195–10212.

(65) Canner, S. W.; Feller, S. E.; Wassall, S. R. Molecular Organization of a Raft-like Domain in a Polyunsaturated Phospholipid Bilayer: A Supervised Machine Learning Analysis of Molecular Dynamics Simulations. *J. Phys. Chem. B* **2021**, *125*, 13158–13167.

(66) Cui, Q.; Pal, T.; Xie, L. Biomolecular QM/MM Simulations: What Are Some of the Burning Issues? *J. Phys. Chem. B* **2021**, *125*, 689–702.

(67) Bouquiaux, C.; Tonnelé, C.; Castet, F.; Champagne, B. Second-Order Nonlinear Optical Properties of an Amphiphilic Dye Embedded in a Lipid Bilayer. A Combined Molecular Dynamics-Quantum Chemistry Study. *J. Phys Chem. B* **2020**, *124*, 2101–2019.

(68) Nelson, D. L.; Cox, M. M. *J. Shoulder Elb. Surg.*; 2008; Vol. 20; pp 1016–1024.

(69) Wu, E. L.; Cheng, X.; Jo, S.; Rui, H.; Song, K. C.; Dávila-Contreras, E. M.; Qi, Y.; Lee, J.; Monje-Galvan, V.; Venable, R. M.; Klauda, J. B.; Im, W. CHARMM-GUI Membrane Builder Toward Realistic Biological Membrane Simulations. *J. Comput. Chem.* **2014**, *35*, 1007–2004.

(70) Klauda, J. B.; Venable, R. M.; Freites, J. A.; o'Connor, J. W.; Tobias, D. J.; Mondragon-Ramirez, C.; Vorobyov, I.; Jr., A. D. M.; Pastor, R. W. Update of the

CHARMM All-Atom Additive Force Field for Lipids: Validation on Six Lipid Types. *J. Phys. Chem. B* **2010**, *114*, 7830–7843.

(71) Pastor, R. W.; Jr., A. D. M. Development of the CHARMM Force Field for Lipids. *J. Phys. Chem. Lett.* **2011**, 1526–1532.

(72) Jorgensen, W. L.; Chandrasekhar, J.; Madura, J. D.; Impey, R. W.; Klein, M. L. Comparison of Simple Potential Functions for Simulating Liquid Water. *J. Chem. Phys.* **1983**, 926–935.

(73) Phillips, J. C.; Braun, R.; Wang, W.; Gumbart, J.; Tajkhorshid, E.; Villa, E.; Chipot, C.; Skeel, R. D.; Kalé, L.; Schulten, K. Scalable Molecular Dynamics with NAMD. *J. Comput. Chem.* **2005**, *26*, 1781–1802.

(74) Feller, S. E.; Zhang, Y.; Pastor, R. W.; Brooks, B. R. Constant Pressure Molecular Dynamics Simulation: the Langevin Piston Method. *J. Chem. Phys.* **1995**, *103*, 4613–4621.

(75) Piana, S.; Lindorff-Larsen, K.; Dirks, R. M.; Salmon, J. K.; Dror, R. O.; Shaw, D. E. Evaluating the Effects of Cutoffs and Treatment of Long-range Electrostatics in Protein Folding Simulations. *PLOS ONE* **2012**, *7*, e39918.

(76) Essmann, U.; Perera, L.; Berkowitz, M. L. A Smooth Particle Mesh Ewald Method. *J. Chem. Phys.* **1995**, *103*, 8577–8593.

(77) Frisch, M. J.; Trucks, G. W.; Schlegel, H. B.; Scuseria, G. E.; Robb, M. A.; Cheeseman, J. R.; Scalmani, G.; Barone, V.; Petersson, G. A.; Nakatsuji, H.; Li, X.; Caricato, M.; Marenich, A. V.; Bloino, J.; Janesko, B. G.; Gomperts, R.; Mennucci, B.; Hratchian, H. P.; Ortiz, J. V.; Izmaylov, A. F.; Sonnenberg, J. L.; Williams-Young, D.; Ding, F.; Lipparini, F.; Egidi, F.; Goings, J.; Peng, B.; Petrone, A.; Henderson, T.; Ranasinghe, D.; Zakrzewski, V. G.; Gao, J.; Rega, N.; Zheng, G.; Liang, W.; Hada, M.;

Ehara, M.; Toyota, K.; Fukuda, R. Gaussian 16 Revision A.03. 2016; Gaussian Inc. Wallingford CT.

(78) Anderson, R. R.; Parrish, J. A. The Optics of Human Skin. *J. Invest. Dermat.* **1981**, *77*, 13–19.

(79) Rehman, S.; Balla, N. K.; Seng, E. Y. Y.; Sheppard, C. J. R. In *Optical Fluorescence Microscopy: From the Spectral to the Nano Dimension*; Diaspro, A., Ed.; Springer: Berlin, Heidelberg, 2011; pp 55–74.

(80) Sakudo, A. Near-Infrared Spectroscopy for Medical Applications: Current Status and Future Perspectives. *Clin. Chim. Acta* **2016**, *455*, 181–188.

(81) Sordillo, L. A.; Pu, Y.; Pratavieira, S.; Budansky, Y.; Alfano, R. R. Deep Optical Imaging of Tissue Using the Second and Third Near-Infrared Spectral Windows. *J. Biomed. Opt.* **2014**, *19*, 056004.

(82) Cohen, A. J.; Mori-Sánchez, P.; Yang, W. Challenges for Density Functional Theory. *Chem. Rev.* **2012**, *112*, 289–320.

(83) Suponitsky, K. Y.; Liao, Y.; Masunov, A. E. Electronic Hyperpolarizabilities for Donor-Acceptor Molecules with Long Conjugated Bridges: Calculations versus Experiment. *J. Phys. Chem. A* **2009**, *113*, 10994–11001.

(84) Shalin, N. I.; Fominykh, O. D.; Balakina, M. Y. Effect of Acceptor Moieties on Static and Dynamic First Hyperpolarizability of Azobenzene Chromophores. *Chem. Phys. Lett.* **2019**, *717*, 21–28.

(85) Abegão, L. M. G.; Fonseca, R. D.; Santos, F. A.; Rodrigues, J. J.; Kamada, K.; Mendonça, C. R.; Piguel, S.; Boni, L. D. First Molecular Electronic Hyperpolarizability of Series of π-Conjugated Oxazole Dyes in Solution: An Experimental and Theoretical Study. *RSC Adv.* **2019**, *9*, 26476–26482.

(86) Besalú-Sala, P.; Sitkiewicz, S. P.; Salvador, P.; Matito, E.; Luis, J. M. A New Tuned Range-Separated Density Functional for the Accurate Calculation of Second Hyperpolarizabilities. *Phys. Chem. Chem. Phys.* **2020**, *22*, 11871–11880.

(87) Lescos, L.; Sitkiewicz, S. P.; Beaujean, P.; Blanchard-Desce, M.; Champagne, B.; Matito, E.; Castet, F. Performance of DFT Functionals for Calculating the Second-Order Nonlinear Optical Properties of Dipolar Merocyanines. *Phys. Chem. Chem. Phys.* **2020**, *22*, 16579–16594.

(88) Bersohn, R.; Pao, Y.; Frisch, H. L. Double Quantum Light Scattering by Molecules. *J. Chem. Phys.* **1966**, *45*, 3184 – 3198.

(89) Momany, F. A. Determination of Partial Atomic Charges from Ab Initio Molecular Electrostatic Potentials. Application to Formamide, Methanol, and Formic Acid. *J. Phys. Chem.* **1978**, *82*, 592–601.

(90) Singh, U. C.; Kollman, P. A. An Approach to Computing Electrostatic Charges for Molecules. *J. Comput. Chem.* **1984**, *5*, 129–145.

(91) Mennucci, B.; Cancès, E.; Tomasi, J. Evaluation of Solvent Effects in Isotropic and Anisotropic Dielectrics and in Ionic Solutions with a Unified Integral Equation Method: Theoretical Bases, Computational Implementation, and Numerical Applications. *J. Chem. Phys. B* **1997**, *101*, 10506–10517.

(92) Tomasi, J.; Mennucci, B.; Cammi, R. Quantum Mechanical Continuum Solvation Models. *Chem. Rev.* **2005**, *105*, 2999–3093.

(93) Miertus, S.; Scrocco, E.; Tomasi, J. Electrostatic Interactions of a Solute with a Continuum. A Direct Utilization of Ab Initio Molecular Potentials for the Prevision of Solvent Effects. *Chem. Phys.* **1981**, *55*, 117–129.

(94) Humphrey, W.; Dalke, A.; Schulten, K. VMD: Visual Molecular Dynamics. *J. Molec. Graphics* **1996**, *14*, 33–38.

(95) Michaud-Agrawal, N.; Denning, E. J.; Woolf, T. B.; Beckstein, O. MDAnalysis: a Toolkit for the Analysis of Molecular Dynamics. *J. Comput. Chem.* **2011**, *32*, 2319–2327.

(96) Gowers, R.; Linke, M.; Barnoud, J.; Reddy, T.; Melo, M.; Seyler, S.; Domański, J.; Dotson, D.; Buchoux, S.; Kenney, I.; Beckstein, O. MDAnalysis: A Python Package for the Rapid Analysis of Molecular Dynamics Simulations. Proc. 15th Python Sci. Conf. 2016; pp 98–105.

(97) Ramasubramani, V.; Dice, B. D.; Harper, E. S.; Spellings, M. P.; Anderson, J. A.; Glotzer, S. C. freud: A Software Suite for High Throughput Analysis of Particle Simulation Data. *Comput. Phys. Commun.* **2020**, *254*, 107275.

(98) Smith, P.; Lorenz, C. D. LiPyphilic: A Python Toolkit for the Analysis of Lipid Membrane Simulations. *J. Chem. Theory Comput.* **2021**, *17*, 5907–5919.

(99) Demšar, J.; Curk, T.; Erjavec, A.; Črt Gorup,; Hočevar, T.; Milutinovič, M.; Možina, M.; Polajnar, M.; Toplak, M.; Starič, A.; Štajdohar, M.; Umek, L.; Žagar, L.; Žbontar, J.; Žitnik, M.; Zupan, B. Orange: Data Mining Toolbox in Python. *J. Mach. Learn. Res.* **2013**, *14*, 2349–2353.

(100) Demšar, J.; Leban, G.; Zupan, B. FreeViz an Intelligent Multivariate Visualization Approach to Explorative Analysis of Biomedical Data. *J. Biomed. Inform.* **2007**, *40*, 661–671.

(101) Starke-Peterkovic, T.; Turner, N.; Vitha, M. F.; Waller, M. P.; Hibbs, D. E.; Clarke, R. J. Cholesterol Effect on the Dipole Potential of Lipid Membranes. *Biophys. J.* **2006**, *90*, 4060–4070.

(102) Shrestha, R.; Anderson, C. M.; Cardenas, A. E.; Elber, R.; Webb, L. J. Direct Measurement of the Effect of Cholesterol and 6-Ketocholestanol on the Membrane Dipole Electric Field Using Vibrational Stark Effect Spectroscopy Coupled with Molecular Dynamics Simulations. *J. Phys. Chem. B* **2017**, *121*, 3424–3436.

(103) Nakazawa, I.; Iwaizumi, M. A Role of the Cancer Cell Membrane Fluidity in the Cancer Metastases: An ESR Study. *Tohoku J. Exp. Med.* **1989**, *157*, 193–198.

(104) Tallima, H.; Azzazy, H. M. E.; El Ridi, R. Cell Surface Sphingomyelin: Key Role in Cancer Initiation, Progression, and Immune Evasion. *Lipids Health Dis.* **2021**, *20*, 150.

(105) Kanis, D. R.; Ratner, M. A.; Marks, T. J. Design and Construction of Molecular Assemblies with Large Second-Order Optical Nonlinearities. Quantum Chemical Aspects. *Chem. Rev.* **1994**, *94*, 195–242.

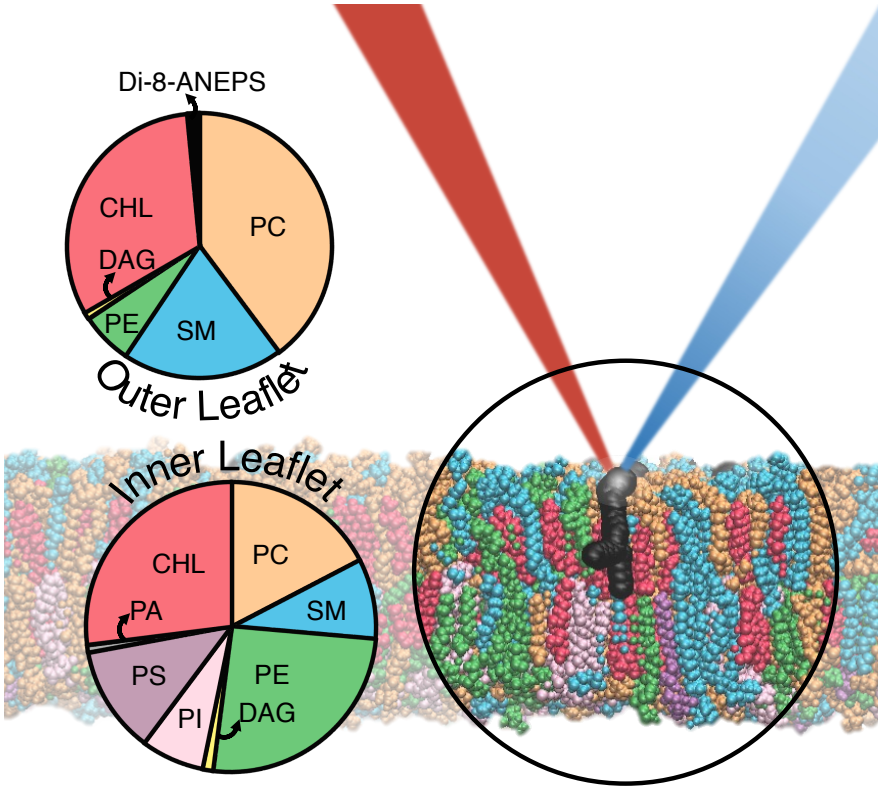

All-atom molecular dynamics simulation of a multi-million atoms membrane mimicking the composition of an ideal plasma membrane containing NLO-active di-8-ANEPPS embedded chromophores.